

Oxidation of a Dispersion-Strengthened Powder Metallurgical FeCrAl Alloy in the Presence of O₂ at 1,100 °C: The Influence of Water Vapour

K. Hellström · N. Israelsson · N. Mortazavi ·
S. Canovic · M. Halvarsson · J.-E. Svensson ·
L.-G. Johansson

Received: 26 November 2014 / Revised: 16 January 2015 / Published online: 4 February 2015
© The Author(s) 2015. This article is published with open access at Springerlink.com

Abstract The oxidation behaviour of the FeCrAl alloy Kanthal[®] APMT in O₂ + N₂ and O₂ + N₂ + H₂O environments at 1,100 °C was investigated using thermogravimetry and detailed analyses of the scale morphology with SEM/EDX and STEM/EDX. Wrought FeCrAl alloy Kanthal[®] AF was used as a reference. Exposure time was up to 168 h. Water vapour influenced the early oxide growth kinetics. This effect is explained in terms of water acting as an oxidant, simultaneously with O₂. During later stages of the exposures, H₂O had no effect on the kinetics of oxidation.

Keywords FeCrAl · High-temperature oxidation · Water vapour

Introduction

The excellent oxidation resistance of FeCrAl alloys at elevated temperatures relies on the formation of a slow-growing and adherent alumina scale. In order to achieve good oxidation properties, small amounts of so-called reactive elements (RE's, *e.g.*, Y, Zr, Hf, La) must be present in the alloy. The RE effect has been studied for a long period of time and is covered in reviews by Whittle and Stringer [1], Quadackers and Singheiser [2], Pint [3], Hou [4] and Chevalier [5]. The RE additions are known to greatly improve scale adherence. In addition, they decrease the rate of oxide

K. Hellström · N. Israelsson (✉) · J.-E. Svensson · L.-G. Johansson
Department of Environmental Inorganic Chemistry, High Temperature Corrosion Centre, Chalmers
University of Technology, 412 96 Gothenburg, Sweden
e-mail: niklas.israelsson@chalmers.se

N. Mortazavi · S. Canovic · M. Halvarsson
Department of Applied Physics, High Temperature Corrosion Centre, Chalmers University of
Technology, 412 96 Gothenburg, Sweden

growth and modify the growth mechanism of the oxide scale to dominant inward oxygen diffusion. Because RE elements have an affinity for oxygen which is at least as great as that of aluminium, the RE elements enter the alumina scale in ionized form. Moreover, because the corresponding ions are large compared to Al^{3+} , they do not dissolve in aluminium oxide. Instead, they invariably segregate to the grain boundaries of the alumina scale. The effect of RE additions on the rate and direction of scale growth is connected to the fact that the growth of the alumina scale involves grain boundary transport of cations and anions.

The RE component in the alloy can be added in elemental form or as oxide dispersion. Adding the REs as oxide dispersion not only improves the oxidation resistance but also the high-temperature mechanical properties such as creep resistance. Thus, the small refractory RE oxide inclusions are quite stable to coarsening and dissolution at high temperature, preventing re-crystallisation of the alloy grains.

The oxidation of FeCrAl alloys >900 °C has been reported to produce a protective two-layered $\alpha\text{-Al}_2\text{O}_3$ scale, the top layer being outward grown and the bottom layer being inward grown by oxygen ion diffusion [6–12]. In addition, the interface between the two layers has been reported to correspond to the original metal surface. The interface is enriched in Cr which is believed to have entered the scale during transient oxidation [13].

The influence of water vapour on the rate of oxidation of FeCrAl alloys in the presence of O_2 has been investigated by several researchers [9, 13–16]. However, the reports are somewhat contradictory. Some researchers report lower oxidation rates in the presence of water vapour [9, 16] while others report that water vapour accelerates oxide growth [13, 17, 18].

The present study investigates the oxidation behaviour of the dispersion strengthened powder metallurgical FeCrAl alloy Kanthal[®] APMT at 1,100 °C in $\text{O}_2 + \text{N}_2$ and in $\text{O}_2 + \text{N}_2 + \text{H}_2\text{O}$ environments. The purpose is to shed new light on the effect of water vapour on the oxidation behaviour of FeCrAl alloys and on the oxidation behaviour of the PM alloy Kanthal[®] APMT in particular. The study includes an investigation of the oxidation kinetics and a detailed microstructural investigation of the alumina scales formed. A wrought FeCrAl alloy, Kanthal[®] AF is included for reference. Because the exposures are isothermal and as the investigated alloys were RE doped having RE/S ratios $\gg 1$, the role of S on scale adhesion is not addressed.

Experimental Procedures

Material

The dispersion-strengthened powder metallurgical FeCrAl alloy Kanthal[®] APMT was studied and compared with the wrought FeCrAl alloy Kanthal[®] AF. Alloy APMT is a rapidly solidified powder (RSP) alloy which contains small refractory inclusions of oxides, carbides and nitrides homogeneously dispersed in the FeCrAl matrix. For further information, see [19, 20]. Alloy AF is manufactured using a

conventional melting technique, followed by hot-rolling, pickling and cold-rolling. The chemical compositions of the alloys are given in Table 1.

The material was supplied by Sandvik Heating Technology in the form of a 2 mm thick sheet, from which square samples ($1.5 \times 1.5 \text{ cm}^2$) were prepared. These were ground and polished with a $1 \mu\text{m}$ diamond suspension in the final step. The samples were cleaned in ethanol using ultrasonic agitation, and then rinsed first in acetone and finally in ethanol. The samples were subsequently dried in flowing air and weighed on a six-decimal Sartorius balance prior to exposure.

Oxidation Exposure

Ex-Situ

Oxidation was conducted for 1, 24, 72 and 168 h at $1,100 \text{ }^\circ\text{C}$ in dry (5 % O_2 + 95 % N_2) and humid (5 % O_2 + 55 % N_2 + 40 % H_2O) environments. The samples were mounted on an alumina holder positioned parallel to the direction of the gas flow in a tube furnace fitted with an alumina tube. At the start of the exposure, the samples were inserted into a hot furnace to limit the heat-up time. The gas flow rate was 1,000 ml/min which correspond to a net gas flow velocity of 3.2 cm/s. Water vapour was generated by passing the dry gas through heated water and then using a cooling system in order to reach the desired dew point. After exposure, the samples were allowed to cool in dry air. The samples were stored in a desiccator before analysing of the oxide scales.

In-Situ

Oxidation experiments were carried out in a thermobalance, (Setaram TAG) in order to investigate the oxidation kinetics. The mass gain and temperature were monitored throughout the exposure and recorded continuously during the isothermal exposure at $1,100 \text{ }^\circ\text{C}$ for 72 h. The exposures were conducted in flowing gas (5 % O_2 + 95 % N_2 and 5 % O_2 + 40 % H_2O + 55 % N_2) at a flow rate of 15 ml/min (0.3 cm/s).

The thermobalance comes equipped with a double symmetrical furnace, in which an Al_2O_3 sample with the same dimension as the sample of interest was used as a reference in order to reduce the buoyancy effects. The specimens were heated at $99 \text{ }^\circ\text{C}/\text{min}$ to $1,100 \text{ }^\circ\text{C}$ and then isothermally exposed for 72 h. In addition to the thermo gravimetric measurements, the mass of each specimen was measured before and after exposure to verify the obtained mass gains. At least two identical

Table 1 The nominal chemical composition of Kanthal[®] APMT and Kanthal[®] AF, given in wt%

Element (wt%)	Fe	Cr	Al	Mo	Mn	Si	C	S	RE
APMT	Bal.	21.0	5.0	3.0	≤ 0.4	≤ 0.7	≤ 0.08	< 0.002	Y, Zr, Hf, Ti
AF	Bal.	20.5–23.5	5.3	–	≤ 0.4	≤ 0.7	≤ 0.08	< 0.002	Y, Zr

exposures were carried out at each exposure environment to validate the results. The data were plotted from the time point at which the isothermal exposure temperature was reached.

In-Situ Versus Ex Situ Exposures

It should be noted that there exist certain differences in the mass gain measured in situ (TGA exposures) and ex situ (tube-furnace exposures). The TGA exposures started in a cool furnace which was then ramped to temperature at 99 °C/min (11 min in total). The TGA measurement data were only collected after 1,100 °C was reached because of the buoyancy effects that occur during the heating period. In contrast, mass gain from the tube furnace exposures includes the mass gain during heat-up. In the tube furnace exposures, the samples were inserted into a hot furnace and, consequently, will heat up faster than in the TG. The sizes of the samples were also different so that the TG-exposed samples had relatively higher fraction of rim area than the furnace-exposed samples. The net gas velocity in the TG exposure was about 10 % of the value in the furnace exposure. These differences may influence both growth kinetics and the oxidation microstructure. The microscopy was performed on samples exposed in the tube furnace.

X-ray Diffraction (XRD)

The crystalline phases of the grown oxide were analysed using Grazing Incidence X-ray diffraction (GI-XRD) (for alloy APMT) and using Bragg–Brentano (BB) XRD (for alloy AF). A Siemens D5000 powder diffractometer with Cu-K α radiation was used. Measurements were performed between 20° < 2 θ < 60° (incidence angle = 0.5°, step size = 0.05°).

Scanning Electron Microscopy with Energy Dispersive X-ray Spectroscopy (SEM/EDX)

The samples were investigated using a FEI Quanta 200 FEG-ESEM operated in high vacuum mode. The instrument comes equipped with an Oxford INCA EDX system. Imaging and EDX analyses were performed at an accelerating voltage of 10–20 kV. Some samples were cast in Bakelite resin with carbon filler in order to prepare cross-sections. The cross-sections were ground and polished down to 1 μ m, and were finishing with a ¼ μ m silica suspension.

Focused Ion Beam/Scanning Electron Microscopy (FIB/SEM)

STEM samples were prepared by a focus ion beam (FIB) in situ lift-out technique using an FEI Strata DB 235 M FIB-SEM.

Scanning Transmission Electron Microscopy (STEM)

Detailed microstructural information was acquired using Scanning Transmission Electron Microscopy (STEM). This study used a Titan 80-300 TEM/STEM equipped with a Field Emission Gun (FEG) that operates at an accelerating voltage of 300 kV was used. The microscope comes equipped with an Oxford Inca EDX detector, and was used to create STEM images in Bright Field (BF) and High Angle Annular Dark Field (HAADF) modes, EDX spot analyses and line-scans.

Transmission-Electron Backscattered Diffraction (t-EBSD)

High spatial resolution crystal structure analysis was performed with transmission-Electron Backscattered Diffraction (t-EBSD), which was performed on the FIB-thinned samples using an HKL Channel 5 EBSD system with a Nordlys II detector. In contrast to conventional EBSD, the foil was tilted 15° away from the phosphor screen and a shorter working distance (3.5 mm) was chosen. A Zeiss Ultra 55 FEG SEM was used in the high current mode with an acceleration voltage of 30 kV and an aperture size of 120 μm .

Results

Alloy Microstructure

Figure 1 shows micrographs of alloys APMT and AF before exposure. In the as-produced state, alloy APMT has much smaller alloy grains (≤ 1 to ~ 5 μm) than alloy AF (10–20 μm). Figure 1c shows a micrograph of alloy APMT after 1 h exposure at 1,100 $^\circ\text{C}$ in O_2 , showing a grain size comparable to alloy AF. As expected, the distribution and size of RE particles in the two alloys differs. The RE particles in alloy APMT are much smaller than in alloy AF (see bright spots in Fig. 1b, c). The RE particles in alloy APMT ranged in size from <100 nm up to 0.5 μm while the typical size in alloy AF was 0.5–3 μm . SEM/EDX analyses revealed that the larger RE particles in alloy APMT tended to be rich in Y, whereas

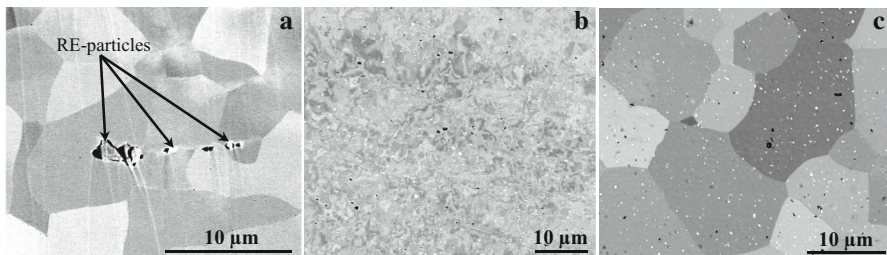


Fig. 1 SEM-BSE images of polished unexposed alloy AF (a) and alloy APMT (b), and alloy APMT exposed for 1 h at 1,100 $^\circ\text{C}$ (c)

the smaller ones were usually dominated by Hf and/or Zr. Small amounts of Ti were present in both alloys. In alloy APMT, Ti was mainly associated with Hf and Zr. In alloy AF, Ti was found in the RE particles together with Y and Zr.

Oxidation Kinetics

Figure 2 shows mass gain as a function of time for the two alloys at 1,100 °C in $O_2 + N_2$ and $O_2 + N_2 + H_2O$ environments. While all four curves show protective oxidation behaviour, the mass gains are slightly higher for the AF material and in the presence of water vapour. The oxidation kinetics is roughly parabolic for both alloys.

Phase Composition of the Scales

Figures 3 and 4 show X-ray diffractograms for both alloys after oxidation in $O_2 + N_2$ environment. Corundum, $\alpha-Al_2O_3$, was the dominant crystalline product

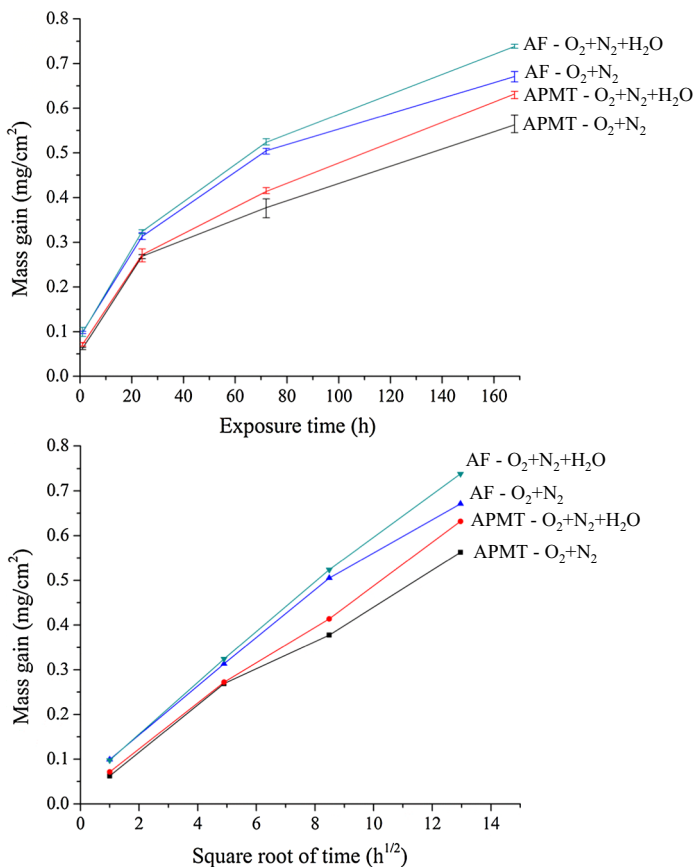


Fig. 2 Mass gain versus exposure time and Mass gain versus square root of exposure time for alloy AF and alloy APMT exposed at 1,100 °C in $O_2 + N_2$ and $O_2 + N_2 + H_2O$ environments

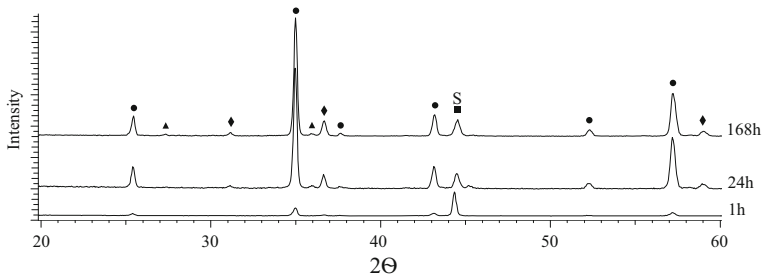


Fig. 3 XRD from alloy AF exposed for 1, 24 and 168 h in O₂ + N₂. The diffractograms obtained in O₂ + N₂ + H₂O were essentially the same. The symbols indicate: α-Al₂O₃ (filled circle), MgAl₂O₄ (filled diamond), TiO₂ (filled triangle), and substrate (filled square)

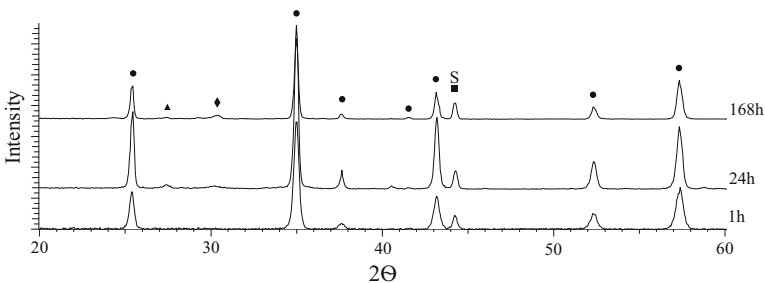


Fig. 4 X-ray diffraction from alloy APMT exposed for 1, 24 and 168 h in O₂ + N₂. The diffractograms obtained in O₂ + N₂ + H₂O were essentially the same. The symbols indicate: α-Al₂O₃ (filled circle), (Zr,Y,Hf)O₂ (filled diamond), TiO₂ (filled triangle), and substrate (filled square)

after all exposure times. In addition, MgAl₂O₄ and TiO₂ were detected on alloy AF while TiO₂ and (Zr,Y,Hf)O₂, were identified on alloy APMT. The presence of water vapour did not influence the phases detected with XRD, however, see below about the identification of a cubic alumina phase detected by t-EBSD on APMT after 168 h in O₂ + N₂ + H₂O environment.

Top View SEM/EDX

The top-view SEM images of the oxidised surface of the two alloys show mostly equi-axed grains in both environments (Figs. 5 and 6), the crystallite size increasing with exposure time. Based on XRD and SEM/EDX, it was concluded that the equi-axed grains consisted of α-alumina. The Al₂O₃ grains were larger on alloy AF than on APMT. For both alloys, the average crystallite size was larger in the presence of water vapour, especially in the early stages of the exposure. The α-alumina crystallites ranged in size from <100 nm on APMT after 1 h in dry environment to approximately 1 μm after 168 h on AF in humid environment.

Alloy AF also exhibited relatively large faceted crystallites on the surface (Fig. 5). SEM/EDX point analysis, showing ~30 at.% Al, ~10 at.% Mg and ~60 at.% O, together with the XRD analysis (Fig. 3), implies that these crystallites

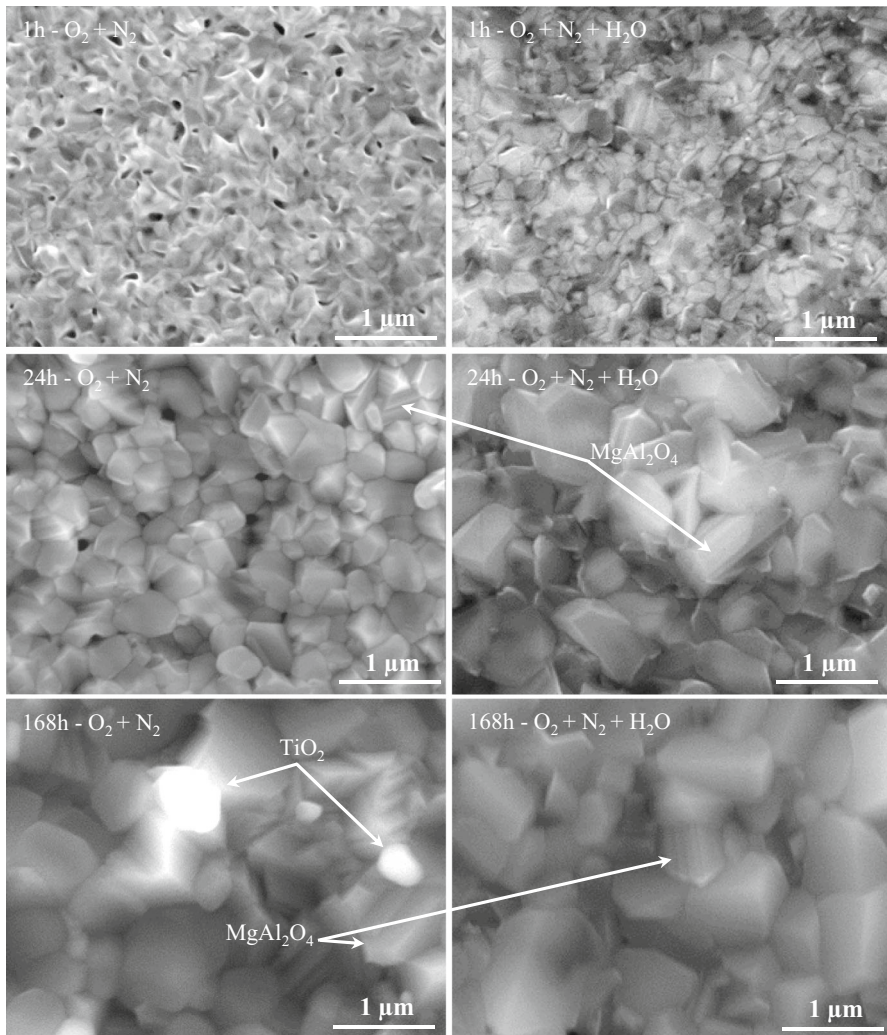


Fig. 5 Top-view SEM-SE images of alloy AF after 1–168 h exposure in $O_2 + N_2$ and $O_2 + N_2 + H_2O$ environments at 1,100 °C

consisted of MgAl spinel oxide ($MgAl_2O_4$). The spinel oxide grains grow with time. The distribution of MgAl spinel in the scale on alloy AF is illustrated by the SEM/EDX Mg map in Fig. 7. Figure 5 also shows that alloy AF formed Ti-rich oxide particles of about 0.5 μm in size (indicated by arrows). These particles most likely correspond to TiO_2 which was identified by XRD. Figure 7 shows that the titanium oxide particles in the scale are less frequent than the spinel, being associated with Y and Zr.

Figures 7 and 8 show top-view SEM images and EDX elemental maps of the two alloys after 24 h exposure in $O_2 + N_2$. The analyses after exposure in

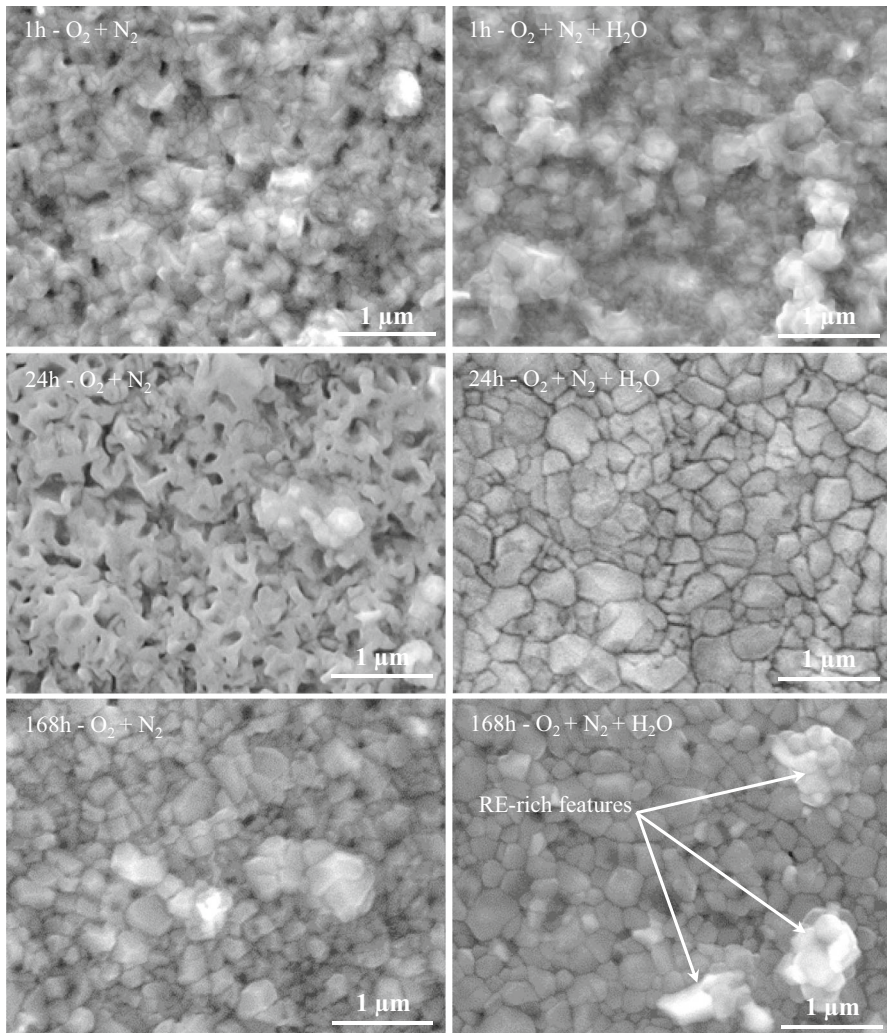


Fig. 6 Top-view SEM-SE images of alloy APMT after 1–168 h exposure in $O_2 + N_2$ and $O_2 + N_2 + H_2O$ environments at 1,100 °C

$O_2 + N_2 + H_2O$ environment yielded similar results (not shown). Based on the mass gain measurements (Fig. 2) and the scale thickness observed in cross sections (see below), it is assumed that the SEM/EDX analyses do not contain information from the alloy substrate, as the EDX information depth is smaller than the scale thickness. Figure 7 (alloy AF) shows white areas (a few μm in diameter) in the micrograph that correspond to RE particles, containing Ti, Y and Zr. The RE particles are assumed to be oxidized. Figure 7 also shows a high density of Mg-rich particles, which most likely correspond to spinel oxide, *c.f.* above. Figure 8 (alloy APMT) also shows RE-rich surface nodules (in this case containing Y and Zr). In

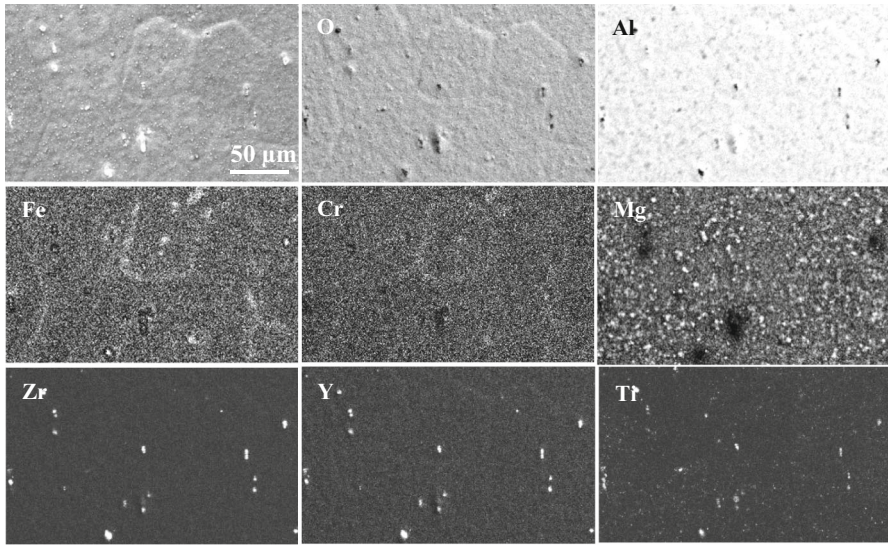


Fig. 7 SEM-SE image and EDX elemental maps of alloy AF after 24 h exposure in $O_2 + N_2$. The nodules seen in the micrograph were rich in RE's (Ti, Y and/or Zr)

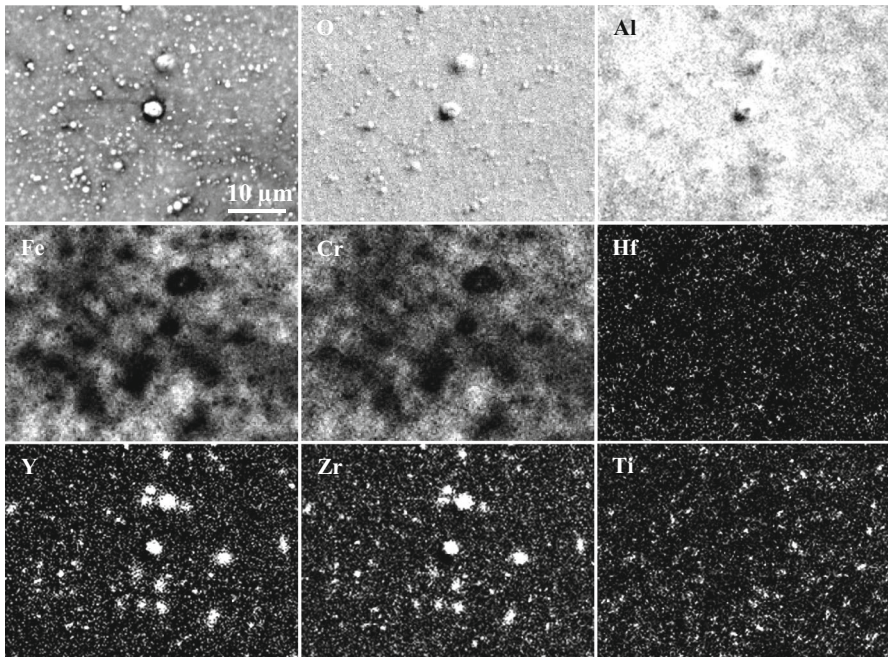


Fig. 8 SEM-SE image and EDX elemental maps of alloy APMT after 24 h exposure in $O_2 + N_2$. The nodules seen in the micrograph were rich in Ti and RE's (Y, Zr, Hf)

addition, the elemental maps in Fig. 8 reveal that Ti and Hf are present in smaller particles evenly dispersed over the oxide surface (top view).

Cross Section SEM/EDX

The cross-sections in Fig. 9 (alloy AF) and 10 (alloy APMT) were prepared after 1, 24 and 168 h exposure, showing that the two alloys have formed a two-layered alumina scales in both dry and humid environments. The two layers in the scale are separated by a relatively straight interface, presumably corresponding to the original sample surface. The interface between the two layers is often associated with pores. In all cases, most of the scale growth took place in the bottom alumina layer, which is dominated by columnar grains. There was no evidence of porosity at the scale/alloy interface.

The top part of the alumina scales formed on APMT was thinner than on alloy AF (compare Figs. 9, 10). Figure 11 depicts a micrograph of a cross-section of alloy AF after 168 h in $O_2 + N_2 + H_2O$, with corresponding EDX elemental maps. In accordance with Fig. 7, the top part of the scale is seen to be enriched in Mg, reflecting the occurrence of MgAl spinel oxide (see above). Figure 12 summarizes the thickness of the top and bottom parts of the alumina scale on the two alloys observed in the cross sections. The total scale thickness was in fair agreement with

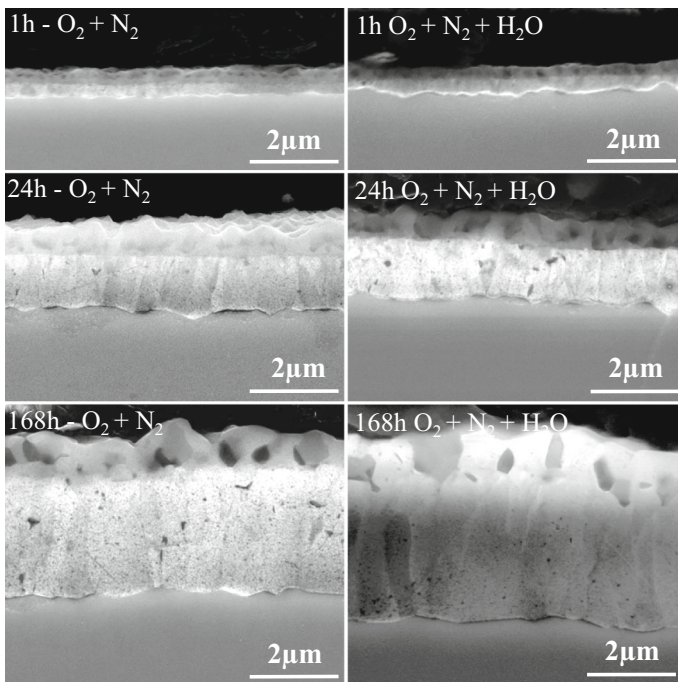


Fig. 9 SEM-SE images of cross-sections of alloy AF after 1–168 h exposure in $O_2 + N_2$ (left) and $O_2 + N_2 + H_2O$ (right) which shows a two-layered oxide scale with columnar grains in the bottom layer

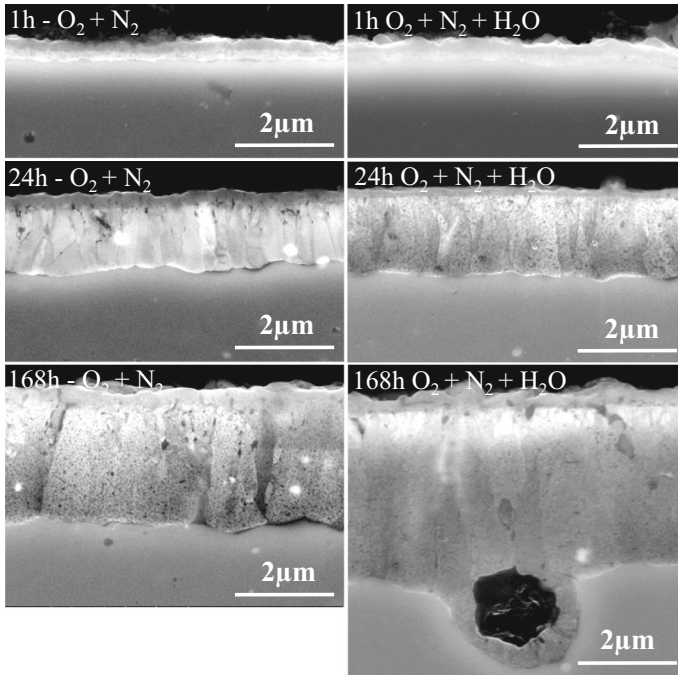


Fig. 10 SEM-SE images of cross-sections of alloy APMT after 1–168 h exposure in $O_2 + N_2$ (*left*) and $O_2 + N_2 + H_2O$ (*right*), which shows a two-layered oxide scale with columnar grains in the bottom part

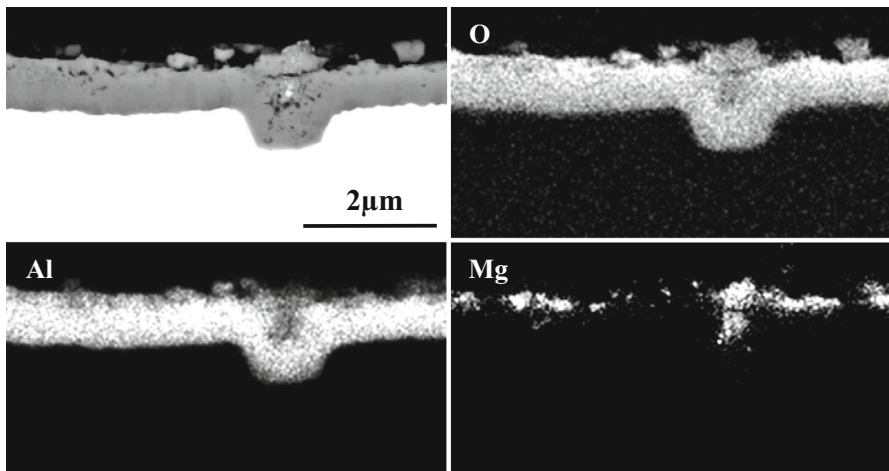


Fig. 11 SEM-BSE image and EDX elemental maps of a cross-section of alloy AF exposed for 168 h in $O_2 + N_2 + H_2O$, which shows the distribution of Mg, Al and O

the average scale thickness calculated from the recorded mass gains (Fig. 2) for pure, 100 % dense alumina. After 168 h exposure, the mass gains of alloy APMT corresponded to the average scale thicknesses of 3.0 and 3.4 μm in dry and humid

environments respectively. The corresponding values for alloy AF were 3.6 and 3.9 μm .

While Fig. 12 shows that both alloys formed thicker scales in the presence of H_2O , it may be noted that the presence of water caused the top scale layer to become thicker on alloy AF. In contrast, the presence of water resulted in additional growth of the bottom scale layer of alloy APMT. Moreover, while the top scale layer on APMT did not grow much with time, the top scale layer on AF grew significantly with exposure time. This was especially apparent in humid environment. Thus, the top layer was 0.15–0.25 μm on APMT in both environments. On alloy AF, the thickness of the top layer increased from about 0.25 μm after 1 h to $\sim 1.0 \mu\text{m}$ after 168 h in dry environment and to $\sim 1.5 \mu\text{m}$ in the presence of H_2O .

Detailed Kinetics Analysis

Figure 13 shows in situ TGA measurements of alloy APMT in $\text{O}_2 + \text{N}_2$ and $\text{O}_2 + \text{N}_2 + \text{H}_2\text{O}$ environments. Similar to the ex situ measurements (Fig. 2), the oxidation rate was somewhat higher in the presence of water vapour. Figure 13 also shows an $\ln(\text{mass gain})$ versus $\ln(\text{time})$ plot, starting after about 20 min at 1,100 $^\circ\text{C}$ (the earlier data was excluded because of scatter). The slope of the $\ln(m)/\ln(t)$ plot corresponds to $1/\alpha$ where α is the exponent in the kinetic expression:

$$m^\alpha \propto t \tag{1}$$

Thus, a constant (linear) mass gain corresponds to $\alpha = 1$ while parabolic growth corresponds to $\alpha = 2$. Figure 13 shows that oxidation kinetics were close to

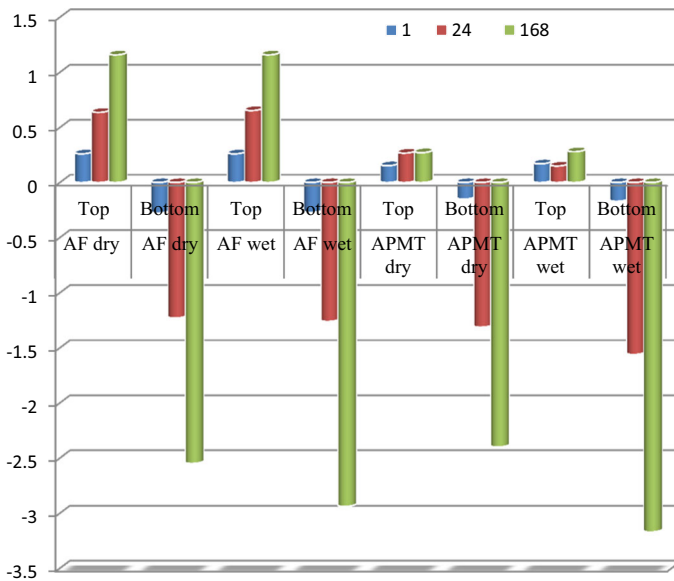


Fig. 12 The average top and bottom oxide layer thickness (μm) of alloy APMT and alloy AF after 1, 24 and 168 h exposure in $\text{O}_2 + \text{N}_2$ and $\text{O}_2 + \text{N}_2 + \text{H}_2\text{O}$

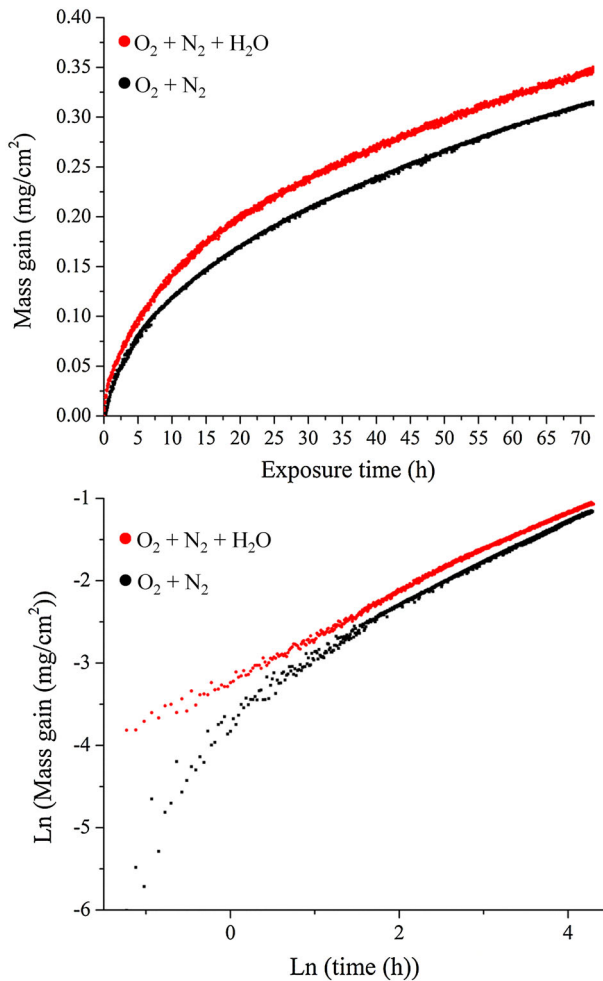


Fig. 13 In situ TGA measurement showing mass gain versus exposure time (*upper graph*) for alloy APMT exposed at 1,100 °C in O₂ + N₂ and O₂ + N₂ + H₂O environment. The data was logarithmised (*lower graph*) in order to evaluate the kinetics

parabolic in the O₂ + N₂ + H₂O environment throughout the entire exposure. The oxidation kinetics slowed down with time from parabolic to sub-parabolic (see Table 2). In contrast, in O₂ + N₂ environment, the slope was initially steeper, corresponding to $\alpha \ll 2$ and became parabolic after about 7 h. The k_p (parabolic oxidation) was quite similar for both environments, about $4 \times 10^{-13} \text{ g}^2/\text{cm}^4 \text{ s}$ between 24 and 72 h (Table 2).

Detailed Microstructural Analysis of the Scale

STEM and t-EBSD were performed on thin-foil samples in order to investigate the microstructure of the scales formed on alloy APMT in more detail. Cross-section

Table 2 Parabolic rate constants and α for Reaction (1), originating from the TG data for alloy APMT from Fig. 13

Ex-situ (tube furnace)				
k_p – APMT ($O_2 + N_2$)	$k_p = 5 \times 10^{-13} \text{ g}^2/\text{cm}^4 \text{ s}$			
k_p – APMT ($O_2 + N_2 + H_2O$)	$k_p = 6 \times 10^{-13} \text{ g}^2/\text{cm}^4 \text{ s}$			
k_p – AF ($O_2 + N_2$)	$k_p = 7 \times 10^{-13} \text{ g}^2/\text{cm}^4 \text{ s}$			
k_p – AF ($O_2 + N_2 + H_2O$)	$k_p = 9 \times 10^{-13} \text{ g}^2/\text{cm}^4 \text{ s}$			
In-situ (TGA)				
Time period (h)	<1	1–7	7–24	24–72
α ($O_2 + N_2$)	0.6	1.5	1.9	2.1
k_p ($O_2 + N_2$)				$3.8 \times 10^{-13} \text{ g}^2/\text{cm}^4 \text{ s}$
α ($O_2 + N_2 + H_2O$)	1.9	1.8	2.0	2.3
k_p ($O_2 + N_2 + H_2O$)				$4.3 \times 10^{-13} \text{ g}^2/\text{cm}^4 \text{ s}$

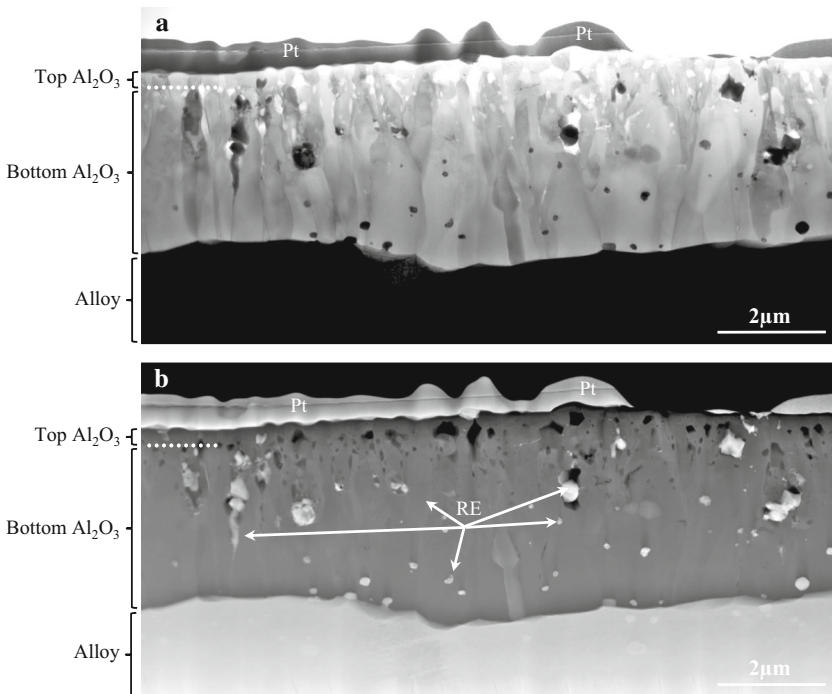


Fig. 14 STEM micrographs **a** BF and **b** HAADF of a cross-section of alloy APMT exposed in $O_2 + N_2$ for 168 h at 1,100 °C. The alloy substrate, alumina scale and the Pt-layer deposited during specimen preparation can be seen. Some RE particles are *arrowed*. The *dotted lines* indicate the interface between the top and bottom alumina layers

STEM-BF and -HAADF images of a sample exposed to the $O_2 + N_2$ environment for 168 h are shown in Fig. 14. Remnants of the Pt-layer deposited on top of the scale during thin-foil preparation can be seen. In accordance with Figs. 10 and 12,

the alumina scale is approximately 3 μm thick and consists of a thin top layer and a thicker bottom layer, the top layer having a thickness of about 0.3 μm (the interface between the two layers is indicated by dotted lines). The bottom part of the scale contains RE particles (dark in BF and bright in HAADF) in the range from <0.1 to 0.5 μm in diameter. An inspection of Fig. 14 shows that RE particles are also present in the alloy substrate. While most RE particles in the scale are rounded, others appear elongated. A closer inspection of such a particle (to the left in the two images in Fig. 14) has shown that it consists of a roughly equi-axed “head” and an elongated “tail”. The elongated RE particles are located at alumina grain boundaries while the rounded RE particles are randomly distributed, usually being located within an oxide grain. Porosity (bright in BF and dark in HAADF) was mainly present in the outer parts of the scale, especially at the interface between the top and bottom layers and in the outer part of the bottom layer. There was also some porosity associated with some of the large RE particles. As in the SEM/EDX image (Fig. 10), there is no evidence of pores at the scale/alloy interface. The alumina grains in the top layer are equi-axed with the same size as the layer thickness, i.e., the outer layer is one grain thick. The bottom alumina layer consists of columnar grains which are about three times wider (0.9 μm) at the bottom of the scale than at the top. The height of the grains varies from 1 to 3 μm . Generally, the taller the

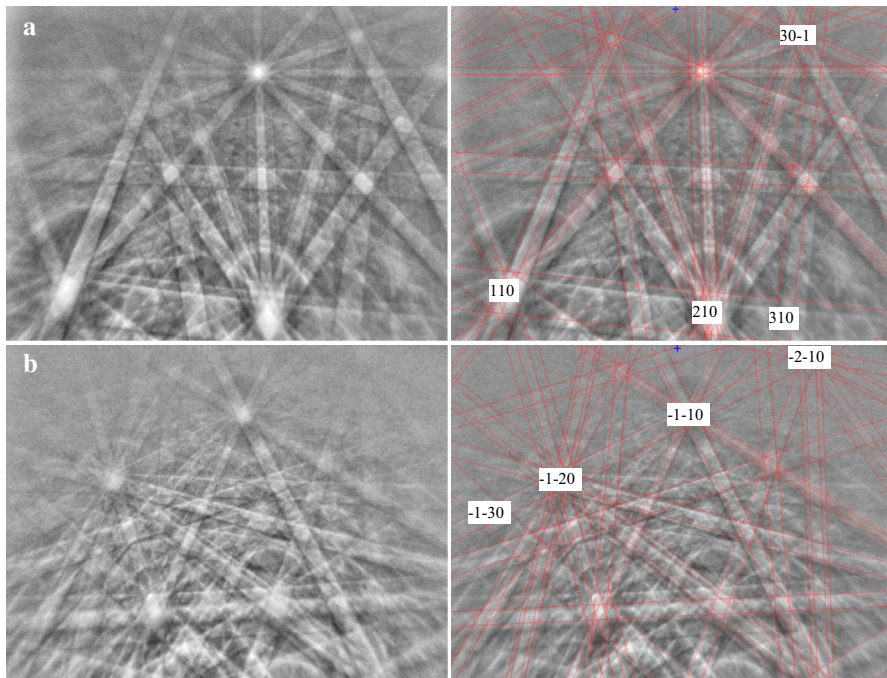


Fig. 15 T-EBSD patterns acquired from the top (a) and bottom (b) alumina layer of alloy APMT exposed to the $\text{O}_2 + \text{N}_2$ environment for 168 h at 1,100 $^\circ\text{C}$. Both patterns could be indexed as the corundum structure

grain, the wider it is at its base. Thus, the diameter of the columnar alumina grains increases as they grow inward.

While the bottom alumina layer consisted of nearly 100 at.% Al (cations), the top layer and the interface between the bottom and top layers also contained Cr and Fe. An 800 nm long STEM/EDX line-scan was obtained through the outer part of the bottom layer and the whole top layer (not shown). The line-scan showed that the bottom/top layer interface region was enriched in Cr and Fe, around 1 at.% each, while the outer part of the top layer was only enriched in Fe to about 2 at.%. The crystal structure of the oxide grains in the two layers was examined with *t*-EBSD. In both layers only the corundum structure (rhombohedral) was detected. Two representative *t*-EBSD patterns are shown in Fig. 15, acquired from one grain in the top layer and one in the bottom layer.

An APMT sample exposed in $O_2 + H_2O + N_2$ environment for 168 h was examined by STEM and *t*-EBSD. Figure 16 shows STEM-BF and HAADF micrographs of the oxide scale and the subjacent metal. Again, the scale is two-layered with a thick (3.5 μm) inner layer and a thinner (0.3 μm) outer layer. Similar to the $O_2 + N_2$ environment, the grains in the top layer are equi-axed (in the figure

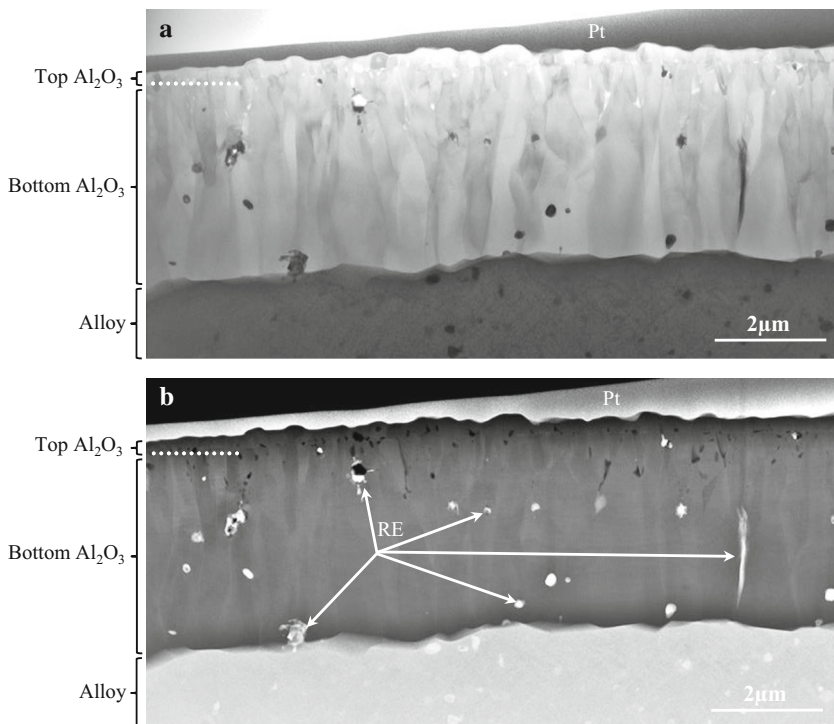


Fig. 16 STEM micrographs **a** BF and **b** HAADF of a cross-section of alloy APMT exposed in $O_2 + N_2 + H_2O$ for 168 h at 1,100 °C. The alloy substrate, alumina scale and the Pt-layer deposited during specimen preparation can be seen. Some RE particles are arrowed. The dotted lines indicate the interface between the top and bottom alumina layers

the layer is one grain thick) while they are columnar in the bottom layer, typically 1–3 μm high and up to 1 μm wide. There is evidence of grain growth in the bottom layer, the alumina grains becoming fewer as the scale/alloy interface is approached. While the porosity is lower than in the dry environment, the pores are distributed in the same way, being located mainly in the outer part of the bottom layer, at the interface between the bottom and top layers, and at large RE particles. The distribution, size, and position of the RE particles in the oxide layer was similar as after exposure in $\text{O}_2 + \text{N}_2$ environment. For instance, an elongated RE particle which is situated at a grain boundary is seen to the right in the two images shown in Fig. 16.

Similar to the samples exposed in $\text{O}_2 + \text{N}_2$, t-EBSD analysis revealed that the grains in both the bottom and top layers were corundum (see Fig. 17). However, one grain in the outer layer, indicated by a cross in Fig. 18a, exhibited a cubic structure, see Fig. 18b. With EDX it was determined that the Fe content of this grain was 10 at.% (90 at.% Al), compared to a typical value of 2 at.% in the neighbouring grains.

The chemical composition of the grain boundaries of the alumina scale was examined in more detail. Figure 19 shows two STEM/EDX spectra; one from an alumina grain boundary and one from a position within an alumina grain, 15 nm

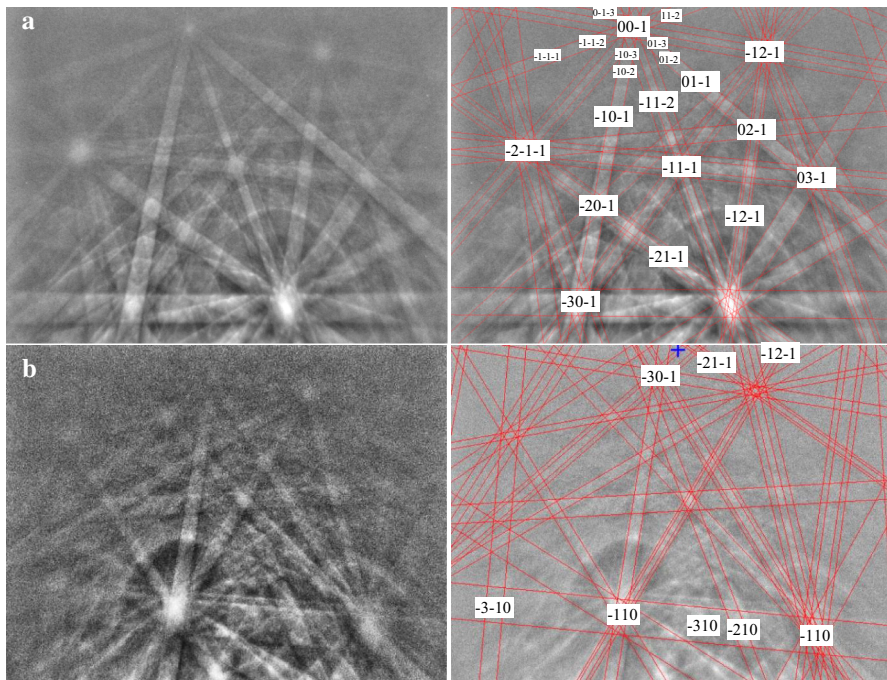


Fig. 17 T-EBSD patterns acquired from the **a** top and **b** bottom alumina layer of alloy APMT exposed to the $\text{O}_2 + \text{N}_2 + \text{H}_2\text{O}$ environment for 168 h at 1,100 $^\circ\text{C}$. The patterns could be indexed as the corundum structure

away from the alumina grain boundary. Thus, Y was found at the alumina grain boundary, while no Y could be detected 15 nm into the grain. It may be noted that Y was only found at some of the alumina grain boundaries in the scale.

Discussion

The investigation of scale cross-sections of samples with SEM/EDX and STEM/EDX (Figs. 9, 10, 14, 16) showed that in all cases (1–168 h, $O_2 + N_2$ and $O_2 + N_2 + H_2O$, APMT and AF) the alumina scale consisted of two layers separated by a relatively straight interface. Both the top and bottom layers consisted of α -alumina. While the top layer consisted of equi-axed alumina grains, the oxide grains in the bottom layer were columnar. Similar scale structures have been reported for FeCrAl alloys by [9, 13, 21–23]. It is proposed that the top alumina layer has grown by the outward diffusion of cations, that the bottom layer has grown by the inward diffusion of oxygen ions and, consequently, that the interface between the two layers corresponds to the original metal surface. The enrichment of Cr and Fe observed at that interface is assumed to be a remnant of transient oxidation, *i.e.*, the contaminants have entered the scale during sample heat-up. Similar enrichments have been reported for alloy APMT at 900–1,100 °C using SIMS and TEM/EDX [13, 21–23]. In the present study, the concentrations of Cr and Fe observed in the scale were much lower than reported by Engkvist et al. at 900 °C [13]. This is suggested to be due the higher exposure temperature that shortens the period of

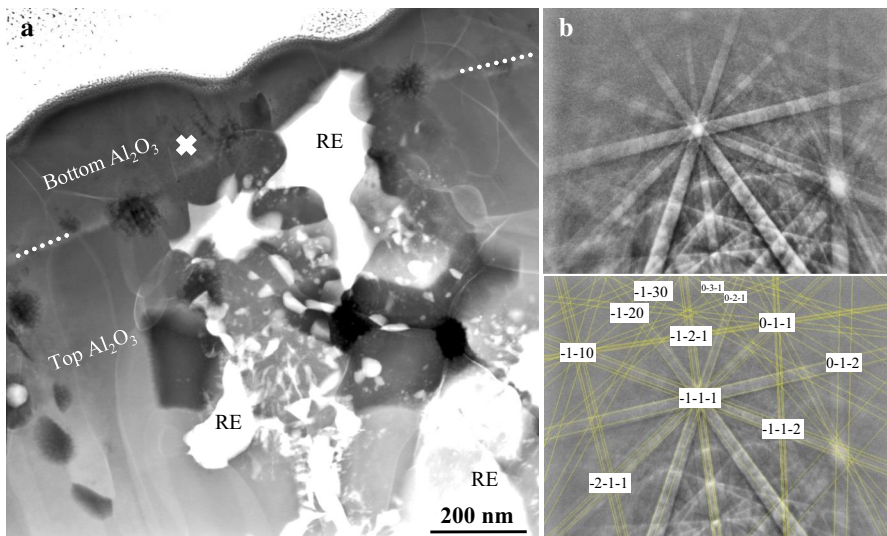


Fig. 18 **a** STEM-HAADF micrograph of the cross-section of alloy APMT exposed to the $O_2 + N_2 + H_2O$ environment for 168 h at 1,100 °C. The cross indicate the position of a grain with a cubic crystal structure in the outer layer, as indicated by the **b** t-EBSD patterns. All other alumina grains exhibited the corundum structure

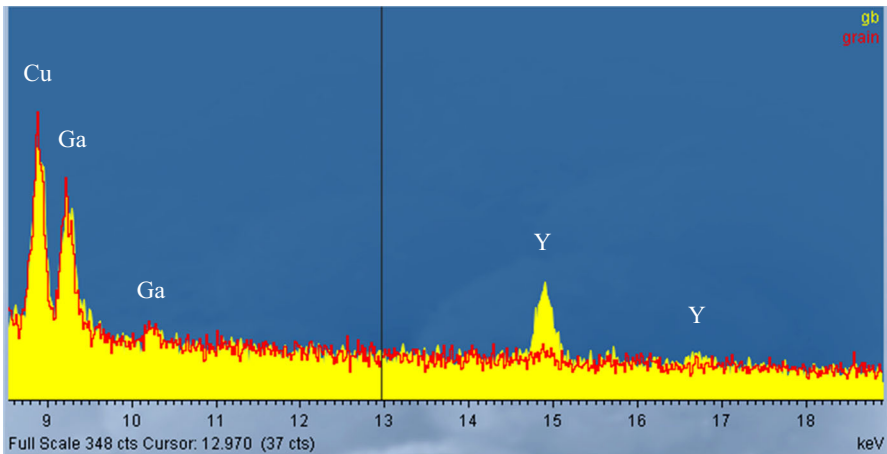


Fig. 19 STEM-EDX spectra from a alumina grain boundary (*filled spectrum area*) and 15 nm away from the alumina grain boundary inside the alumina grain (*line spectrum*). The grain boundary contained yttrium. Cu originates from the TEM grid and Ga from the FIB/SEM sample preparation. (Alloy APMT exposed to the $O_2 + N_2$ environment for 168 h at 1,100 °C)

transient oxidation and increases diffusion rate of Cr and Fe ions within the alumina scale.

The lack of evidence of porosity at the scale/alloy interface (Figs. 10, 14, 16) is in agreement with several reports on the morphology of alumina scales formed on FeCrAl(RE) alloys [3, 4] at this temperature and at 1,200 °C [23]. This is also valid for the reference material (alloy AF, see Fig. 9). While a comparison of the scale microstructure in humid and dry conditions showed relatively small differences, there was clearly more porosity within the scale in the absence of H_2O (Figs. 14, 16). Part of the porosity is associated with the interface between the outward- and inward-growing scale layers. This has also been reported for alloy AF after exposure at 900 °C [21]. Previously, the porosity at the interface between the outward- and inward- growing layers has been attributed to the transformation of metastable alumina formed during transient oxidation to α -alumina [24]. Based on the crystallographic densities of γ -alumina and α -alumina the latter phase change is accompanied by a volume reduction of 7 %. It is suggested that the porosity may also be due to diffusion of Fe and Cr in the transient oxide towards the surface.

The distribution and morphology of the RE particles in the scale appear to be unaffected by the presence of water vapour (Figs. 14, 16). The occurrence of RE particles in the alloy substrate and in the bottom (inward-growing) part of the alumina scale implies that the particles have become included in the scale as a result of oxidation, i.e., because of metal recession. An inspection of Figs. 14 and 16, shows a few RE particles which are in the process of becoming incorporated into the scale in this way. The observation that the RE particles in the upper (older) part of the inward-grown scale tend to be associated with porosity is tentatively attributed to the loss of material from the particles by diffusion of RE ions into the grain boundaries of the scale. The peculiar shape of some RE particles in the scale, i.e.

exhibiting a rounded head and an elongated, nebulous tail, is suggested to reflect the exchange of material between the RE particle and the alloy, as the particle becomes incorporated into the scale. A detailed description of the RE particle “tail” and how it forms is beyond the scope of this paper.

Except for the initial stage (<7 h, see below), a comparison of the mass gains in $O_2 + N_2$ and in $O_2 + N_2 + H_2O$ shows that water had only limited effects on the rate of isothermal oxidation of alloy APMT (see Figs. 2, 13). While the mass gain after 168 h was somewhat greater in the presence of water vapour, oxidation kinetics was nearly parabolic in both environments (Fig. 13), i.e. the corresponding parabolic rate constants were essentially the same (Table 2). The value of k_p is low but within the range reported for alumina-forming alloys at 1,100 °C by Kofstad [25], and in good agreement with values for the FeCrAl alloys reported by Pint [26]. The results from the tube furnace exposures are in line with the TG measurements. Moreover, the furnace exposure measurements show that alloy AF oxidizes slightly faster than alloy APMT (Fig. 2). The limited accelerating effect of water after 168 h is in agreement with a review paper on the water vapour effect by Saunders, Monteiro and Rizzo [14]. The influence of water vapour on oxidation kinetics is discussed below. It is also in accordance with reports in the literature on the oxidation behaviour of alloy APMT at 900, 1,000 and 1,100 °C in $O_2 + H_2O$ and dry O_2 and of alloy AF at 900 °C [13, 27].

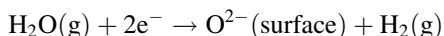
The cross-sections in Figs. 9 and 10 reveal that the relation between the outward- and inward-grown parts of the scale on alloy APMT is different from that of the reference material (alloy AF). The scale thickness measurements in Fig. 12 show that the outward-grown scale is proportionally much smaller for alloy APMT. Also, there was little increase in the outward-grown alumina on alloy APMT with exposure time. In line with the gravimetric data in Figs. 2, 12 shows that the total scale thickness (= inward-grown scale + outward-grown scale) was somewhat greater in $O_2 + N_2 + H_2O$ than in $O_2 + N_2$ environments for both alloys.

The predominantly inward alumina growth of the investigated alloys is in agreement with other studies of RE-containing FeCrAl alloys [12, 23, 28–30]. The different relation between the inward- and outward-grown scale for the two alloys (Fig. 12) is tentatively attributed to the differences in RE additions. Thus, while alloy APMT contains RE's in the form of oxide dispersion, the RE's are added to alloy AF in elemental form. Also, alloy APMT contains Zr, Y and Hf while alloy AF only contains Zr and Y. The detection of Y in the alumina grain boundaries on alloy APMT (Fig. 19) is in agreement with earlier reports on the oxidation microstructure of FeCrAl(Y) alloys and other alumina formers at high temperature [9, 23, 31]. It may be noted that Y was only detected in some alumina grain boundaries.

According to the measurements of mass gain and oxide thickness (Figs. 2, 10, 11 and 14), oxide growth was slightly faster on alloy AF than on alloy APMT in both environments. This may be attributed to differences in microstructure. Before exposure, the grains in APMT are about 10–20 times smaller than the grains of AF (Fig. 1). The smaller grain size most likely increases the Al supply to the surface during initial stages of oxidation, resulting in the faster establishment of a protective alumina scale.

Initially, the presence of water vapour has a major effect on oxidation kinetics, which is evident in the $\ln(\text{mass gain})$ versus $\ln(\text{time})$ plot of TG data in Fig. 13. Thus, while the oxidation kinetics in $\text{O}_2 + \text{N}_2 + \text{H}_2\text{O}$ is parabolic from very early on, the slope of the $\ln(\text{mass gain})$ versus $\ln(\text{time})$ plot was initially >1 in the $\text{O}_2 + \text{N}_2$ environment and only reached 0.5 (corresponding to parabolic kinetics) after about 7 h. Also, the mass gain curve in $\text{O}_2 + \text{N}_2$ is seen to be located below the $\text{O}_2 + \text{N}_2 + \text{H}_2\text{O}$ curve. This means that in the absence of H_2O , the transport of species across the oxide scale only becomes rate limiting at a relatively late stage, implying that the rate of oxidation is initially limited by a surface reaction. It is proposed that the initial rate-limiting reaction in the $\text{O}_2 + \text{N}_2$ environment is the reduction of O_2 on the scale surface. Oxide growth which is limited by a reaction occurring on the surface of constant area and composition would result in linear kinetics (slope of $\ln(\text{mass gain})$ versus $\ln(\text{time}) = 1$). The greater slope (>1) during the early stages of oxidation in the $\text{O}_2 + \text{N}_2$ environment is tentatively attributed to an increasing surface area caused by the formation of an outward-growing transient oxide and/or to an increasing concentration of transition metal ions (i.e. Fe^{2+}) at the scale surface. The presence of transition metal ions at the scale surface is suggested to catalyze oxygen reduction.

In a Wagner-type scenario, in which metal oxidation and the reduction of oxidant occur at the scale/alloy and scale/gas interfaces, respectively, and ions and electrons are transported across a growing dense scale, these differences in early oxidation kinetics imply that the rate of the reduction of oxidant (the cathodic process) is initially faster in $\text{O}_2 + \text{N}_2 + \text{H}_2\text{O}$ environment than in $\text{O}_2 + \text{N}_2$ environment. The simplest explanation for the initial accelerating effect of water vapour is that the reduction of water occurs simultaneous with the reduction of O_2 , and that both processes contribute to metal oxidation:



In line with this idea, Åkermark and Hultquist [32], working with the early stages of oxidation of a FeCrAl alloy in O_2 and H_2O environments, reported that exposure in an $\text{O}_2 + \text{H}_2\text{O}$ environment at 920 °C resulted in the simultaneous reduction of O_2 and H_2O , the reduction of water by the alloy being evidenced by H_2 evolution.

It may be noted that the simultaneous reduction of H_2O and O_2 on the scale surface violates one of Wagner's preconditions for his derivation of parabolic oxide growth kinetics [33], namely that the reactions at the scale/metal and scale/gas interfaces are essentially at equilibrium. Moreover, if the O_2/O^{2-} reaction is close to equilibrium at the scale surface, water cannot be reduced there. After about 7 h, when the period of non-parabolic oxidation in $\text{O}_2 + \text{N}_2$ has ended, the rate of oxidation is essentially the same in the two environments. This implies that water reduction no longer contributes to oxide growth in the $\text{O}_2 + \text{N}_2 + \text{H}_2\text{O}$ environment at this stage. The reason for the cessation of water reduction would be that, because of scale growth, the transport of ions across the scale has become relatively slow in comparison to O_2 reduction at the surface. This will cause the O_2/O^{2-}

reaction on the surface to approach equilibrium, causing the reducing power of the oxide surface to diminish to such an extent that hydrogen evolution is no longer possible.

As an alternative to water being reduced at the scale surface, there is the possibility that water reduction occurs within the scale, having penetrated there via the alumina grain boundaries. In this scenario, water reduction can occur deep in the scale and the scale surface is thus not required to be strongly reducing. Also in this case, the rate of water reduction would be expected to decrease as the scale grows thicker.

As noted above, the TG data in $O_2 + N_2 + H_2O$ show approximately parabolic kinetics from early on in the exposure. However, a closer inspection of Fig. 13 shows a tendency for the slope of the \ln/\ln plot to diminish somewhat towards the end of the exposure (the slope is $1,9 < 1$ h, $1,8$ between 1 and 7 h, $2,0$ between 7 and 20 h and reaches $2,3$ corresponding to $\Delta m = kt^{0,43}$ between 20 and 72 h, see Table 2). It is well-known that “sub parabolic” oxidation kinetics can be expected if the rate of scale growth on a metal is limited by grain boundary diffusion across an oxide that exhibits grain growth [25]. This is because grain growth causes the available grain boundary area to diminish. As noted above, the TEM cross-sections show evidence of grain growth, the alumina grains in the bottom scale layer becoming coarser as they grow inward (Figs. 14 and 16). The effect is similar to, but less marked than that reported by Young et al. [34] for a FeCrAl alloy at $1,200$ – $1,300$ °C. Hence, it is suggested that the small deviation from parabolic kinetics towards the end of exposure is due to alumina grain growth. In the $O_2 + N_2$ environment, the tendency for the slope of the \ln/\ln curve to diminish with time was somewhat less marked (Table 2).

Bearing in mind that the TG curves are not strictly parabolic, it may be noted that the value of the “parabolic rate constant” between 24 and 72 h is essentially the same in the two environments (see Table 2). While the approximately parabolic kinetics implies that transport across the scale is rate determining, the observation that the parabolic rate constant is the same implies that the rate-determining step in the transport across the scale is also the same in the two environments. Consequently, the results indicate that water and hydrogen play no decisive role in the transport across the scale at this stage.

The observation of a cubic oxide grain in the top part of the scale after 168 h in $O_2 + N_2 + H_2O$ (see Fig. 18) is notable. According to STEM/EDX the grain contains 90 % Al and 10 % Fe (cationic). The low iron content means that the grain does not consist of the cubic spinel oxide $FeAl_2O_4$. Instead, the crystal is suggested to consist of metastable alumina. Several metastable aluminas feature a cubic close-packing of oxygen ions and can be described as highly cation-deficient spinel structures (γ , θ , δ). Among them, γ -alumina is cubic [35]. It has also been reported that divalent cations are readily soluble in transient aluminas [36]. Thus, it is proposed that the grain marked in Fig. 18 consists of γ -alumina with dissolved Fe^{2+} . Metastable aluminas are reported to form during early stages of high temperature oxidation of FeCrAl alloys and at intermediate temperatures [21, 22, 37–39]. They are invariably found in the outer part of the scale, and grow by cation (outward) diffusion [40]. As noted above, metastable aluminas on FeCrAl’s easily

transform to α -alumina or to a mixture of α -alumina and spinel oxide [21]. Hence, metastable aluminas are usually reported on FeCrAl's after exposure at lower temperatures (≤ 900 °C) and/or shorter exposure times [17]. Thus, we are unaware of reports of metastable aluminas forming on FeCrAl's at 1,100 °C. It is suggested that the unexpected stability of metastable alumina in the present case is connected to the iron content. Moreover, the occurrence of yttrium in the grain boundaries is considered significant (see Fig. 19). Thus, according to Burtin et al. [41] the transformation of metastable alumina to α -alumina at 1,105 °C is inhibited by large trivalent and four-valent cations, e.g., by La^{3+} and Zr^{4+} . It is suggested that Y^{3+} has a similar inhibitive effect and that the observation of metastable alumina in the scale is due to kinetic stabilization caused by Y^{3+} in the grain boundaries.

Conclusions

- Water vapour influences the early oxidation kinetics of alloy APMT in the presence of O_2 . Thus, the early oxidation kinetics is parabolic in $\text{O}_2 + \text{N}_2 + \text{H}_2\text{O}$. In the $\text{O}_2 + \text{N}_2$ environment, kinetics only become parabolic >7 h.
- It is proposed that, in dry conditions, oxide growth is initially limited by reduction of O_2 at the surface.
- The effect of water vapour on the early oxidation kinetics is attributed to water acting as an oxidant at the scale gas interface, simultaneously with O_2 .
- The kinetics of oxide growth are essentially the same in dry and wet environments >7 h, which implies that water and/or hydrogen does not play an important role in the transport across the scale at this stage.
- The alloy forms a two-layered scale mainly consisting of α -alumina. The top layer is relatively thin and consists of a single layer of equi-axed alumina grains while the grains in the bottom layer are columnar. It is proposed that the top layer has grown by the outward diffusion of cations and that the bottom layer has grown by inward diffusion of oxygen ions. The interface between the top and bottom layers is enriched in Cr and Fe and is proposed to correspond to the original metal surface.
- There is a tendency of the oxide growth kinetics to become slightly sub-parabolic towards the end of the exposure. This is attributed to grain growth in the bottom alumina layer.
- The bottom alumina layer contains RE-rich oxide particles that are also present in the alloy. The particles become incorporated into the scale during oxidation because of metal recession.
- The nebulous tail exhibited by some RE particles in the scale is suggested to reflect the exchange of material between the RE particle and the alloy, as the particle becomes incorporated into the scale.
- Occasionally iron-containing cubic alumina, suggested to be γ -alumina, could be identified in the top alumina layer after 168 h at 1,100 °C.

Acknowledgments This research was conducted at the Swedish High Temperature Corrosion Centre (HTC) at Chalmers University of Technology.

Open Access This article is distributed under the terms of the Creative Commons Attribution License which permits any use, distribution, and reproduction in any medium, provided the original author(s) and the source are credited.

References

1. D. P. Whittle and J. Stringer, *Philosophical Transactions of the Royal Society A* **295**, 309 (1980).
2. W. J. Quadakkers and L. Singheiser, *Material Science Forum* **369–372**, 77 (2001).
3. B. A. Pint, in *Proceedings of the John Stringer Symposium on High Temperature Corrosion*, eds. P.T. Tortorelli, I.G. Wright and P.Y. Hou, Vol. 9 (ASM International, Materials Park, OH, 2003), pp. 9–19.
4. P. Y. Hou, *Materials Science Forum* **696**, 39 (2011).
5. S. Chevalier, *Materials and Corrosion* **65**, 109 (2014).
6. L. Marechal, B. Lesage, A. M. Huntz and R. Molins, *Oxidation of Metals* **60**, 1 (2003).
7. B. A. Pint, A. J. Garratt-Reed and L. W. Hobbs, *Oxidation of Metals* **56**, 119 (2001).
8. M. A. Montealegre, G. Strehl, J. L. González-Carrasco and G. Borchardt, *Intermetallics* **13**, 896 (2005).
9. K. A. Unocic, E. Essuman, S. Dryepondt and B. A. Pint, *Materials at High Temperatures* **29**, 171 (2012).
10. H. Al-Badairy, D. J. Prior and G. J. Tatlock, *Materials at High Temperatures* **22**, 453 (2005).
11. J. R. Blachère, E. Schumann, G. H. Meier and F. S. Pettit, *Scripta Materialia* **49**, 909 (2003).
12. C. Mennicke, E. Schumann, M. Ruhle, R. J. Hussey, G. I. Sproule and M. J. Graham, *Oxidation of Metals* **49**, 455 (1998).
13. J. Engkvist, S. Canovic, K. Hellström, A. Järtnäs, J.-E. Svensson, L.-G. Johansson, M. Olsson and M. Halvarsson, *Oxidation of Metals* **73**, 233 (2010).
14. S. R. J. Saunders, M. Monteiro and F. Rizzo, *Progress in Materials Science* **53**, 775 (2008).
15. H. Essom, *Mécanique & Industries* **4**, 285 (2003).
16. H. Buscaïl, S. Heinze, P. Dufour and J. P. Larpin, *Oxidation of Metals* **47**, 445 (1997).
17. H. Götlind, F. Liu, J.-E. Svensson, M. Halvarsson and L.-G. Johansson, *Oxidation of Metals* **67**, 251 (2007).
18. H. Al-Badairy and G. J. Tatlock, *Materials at High Temperatures* **17**, 133 (2000).
19. B. Jönsson, Q. Lu, D. Chandrasekaran, R. Berglund and F. Rave, *Oxidation of Metals* **79**, 29 (2013).
20. B. Jönsson, R. Berglund, J. Magnusson, P. Henning and M. Hättstrand, *Materials Science Forum* **461–464**, 455 (2004).
21. F. Liu, H. Götlind, J.-E. Svensson, L.-G. Johansson and M. Halvarsson, *Corrosion Science* **50**, 2272 (2008).
22. F. Liu, H. Josefsson, J. E. Svensson, L. G. Johansson and M. Halvarsson, *Materials at High Temperatures* **22**, 521 (2005).
23. B. A. Pint, K. L. More and I. G. Wright, *Materials at High Temperatures* **20**, 375 (2003).
24. B. A. Pint, K. L. More, I. G. Wright and P. F. Tortorelli, *Materials at High Temperatures* **17**, 165 (2000).
25. P. Kofstad, *High Temperature Corrosion*, (Elsevier Applied Science Publishers Ltd, London, 1988).
26. B. A. Pint, *Journal of the American Ceramic Society* **86**, 686 (2003).
27. S. Canovic, J. Engkvist, F. Liu, H. Lai, H. Götlind, K. Hellström, J.-E. Svensson, L.-G. Johansson, M. Olsson and H. Halvarsson, *Journal of the Electrochemical Society* **157**, C223 (2010).
28. D. Clemens, K. Bongartz, W. Speier, R. J. Hussey and W. J. Quadakkers, *Journal of Analytical Chemistry* **346**, 318 (1993).
29. W. J. Quadakkers, A. Elschner, W. Speier and H. Nickel, *Applied Surface Science* **52**, 271 (1991).
30. W. J. Quadakkers, H. Holzbrecher, K. G. Briefs and H. Beske, *Oxidation of Metals* **32**, 67 (1989).
31. B. A. Pint and K. L. More, *Journal of Materials Science* **44**, 1676 (2009).
32. T. Åkermark and G. Hultqvist, *Oxidation of Metals* **47**, 117 (1997).

33. C. Wagner, *Zeitschrift für Physikalische Chemie* **B21**, 25 (1933).
34. D. J. Young, D. Naumenko, L. Niewolak, E. Wessel, L. Singheiser and W. J. Quadackers, *Materials and Corrosion* **61**, 838 (2010).
35. I. Levin and D. Brandon, *Journal of the American Ceramic Society* **81**, 1995 (1998).
36. M. Kusunoki, M. Rokkaku, Y. Ikuhara and H. Yanagida, *Materials Transactions* **39**, 110 (1998).
37. J. R. Nicholls, M. J. Bennett and R. Newton, *Materials at High Temperatures* **20**, 429 (2003).
38. G. Berthomé, E. N'Dah, Y. Wouters and A. Galerie, *Materials and Corrosion* **56**, 389 (2005).
39. G. J. Tatlock, H. Al-Badairy, M. J. Bennett, R. Newton, J. R. Nicholls and A. Galerie, *Materials Science and Technology* **21**, 893 (2005).
40. N. Birks and G. H. Meier, *Introduction to High Temperature Oxidation of Metals*, 2nd ed, (Cambridge University Press, Cambridge, 2006).
41. P. Burtin, J. P. Brunelle, M. Pijolat and M. Soustelle, *Applied Catalysis* **34**, 225 (1987).